ELSEVIER

Contents lists available at ScienceDirect

Applied Catalysis B: Environment and Energy

journal homepage: www.elsevier.com/locate/apcatb



Constructing strong built-in electric field in lead-free halide-perovskite-based heterojunction to boost charge separation for efficient CO₂ photoreduction

Zhao-Lei Liu^a, Yan-Fei Mu^b, Xi-Rui Li^a, You-Xiang Feng^a, Min Zhang^{a,*}, Tong-Bu Lu^{a,*}

ARTICLE INFO

Keywords: Built-in electric field CO₂ reduction Charge transfer Lead-free perovskite Photocatalysis

ABSTRACT

Maximizing the utilization of photogenerated carriers by enhancing the interfacial charge separation efficiency of heterojunctions represents a potent strategy for bolstering their photocatalytic activity. Herein, we report an unprecedented strategy for the construction of halide-perovskite-based heterojunction by combining two semiconductors with distinct semiconducting properties, which is elaborately fabricated by in-situ growth of n-type lead-free halide perovskite $Cs_2AgBiBr_6$ (CABB) onto the surface of p-type porous Co_3O_4 . The pronounced Fermi level disparity between CABB and Co_3O_4 propels the formation of a robust built-in electric field at the CABB/ Co_3O_4 heterojunction interface, which promotes the separation of photogenerated carriers via an S-scheme pathway, thereby significantly enhancing the photocatalytic CO_2 reduction performance. Incorporating Na ions into CABB can further intensify the built-in electric field by diminishing the defect density of CABB to enhance its charge carrier mobility. Consequently, the resultant Na-CABB/ Co_3O_4 heterojunction demonstrates an exceptional electron consumption rate of 1336 µmol $g^{-1}h^{-1}$ for photocatalytic conversion of CO_2 into CO and CH_4 with water as electron source, far surpassing the currently reported lead- and lead-free halide perovskite materials without reliance on any sacrificial agents.

1. Introduction

Artificial photosynthesis is considered a green and sustainable solution to climate challenges, as it can convert CO_2 and H_2O into valuable chemicals on photocatalysts by utilizing solar energy [1–4]. An efficient artificial photosynthesis system should simultaneously possess the abilities for both CO_2 reduction and H_2O oxidation, requiring a sufficiently wide bandgap or energy gap in the photocatalyst to support these reactions. Due to the inherently sluggish kinetics of both CO_2 reduction and H_2O oxidation, the photocatalyst must also possess a prolonged lifetime of photogenerated carriers or excitons to guarantee efficient progress of the reactions. To date, only a handful of materials, such as Co_3O_4 [5], TiO_2 [6,7], $InVO_4$ [8], Cu_2O [9], BiOBr [10,11], C_3N_4 [12, 13], and $NaTaO_3$ [14] among others, can achieve photocatalytic CO_2 reduction using H_2O as an electron donor. Nevertheless, these materials are hindered by limitations like weak visible light-harvesting capability and/or rapid charge recombination, resulting in a substantial decrease

in their photocatalytic CO_2 reduction efficiency. In fact, the majority of current photocatalytic CO_2 reduction systems rely on costly sacrificial agents to eliminate photogenerated holes [15–18], thereby indirectly augmenting their reduction capacity, which undoubtedly imposes an economic burden on practical applications. Consequently, the exploitation of photocatalysts with a robust visible light response and efficient charge separation is highly desired for artificial photosynthesis.

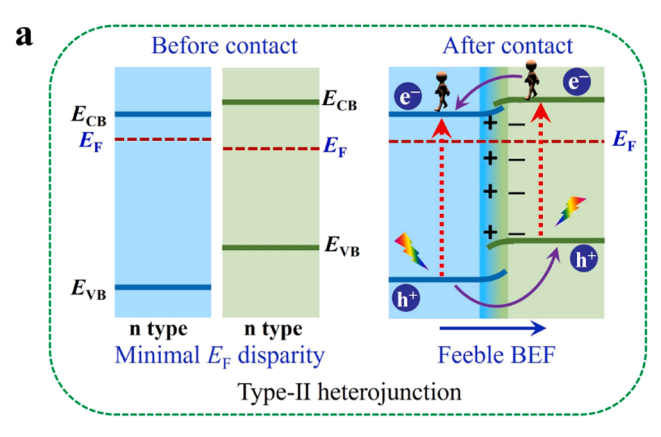
In recent years, halide perovskites (HPs) have shown promise with advantages such as a suitable bandgap, remarkable light absorption, and a long carrier lifetime, enabling wide applications in the field of photocatalysis and photoelectric devices [19–25]. For photocatalytic $\rm CO_2$ reduction, the judicious design of HP-based heterojunctions to ameliorate charge separation, akin to other semiconductor materials, is one of the feasible strategies to enhance the photocatalytic performance [26–30]. Currently, the construction of HP-based heterojunctions primarily involves combining them with other n-type semiconductors, and the photogenerated carriers are separated via either a Type-II [31]

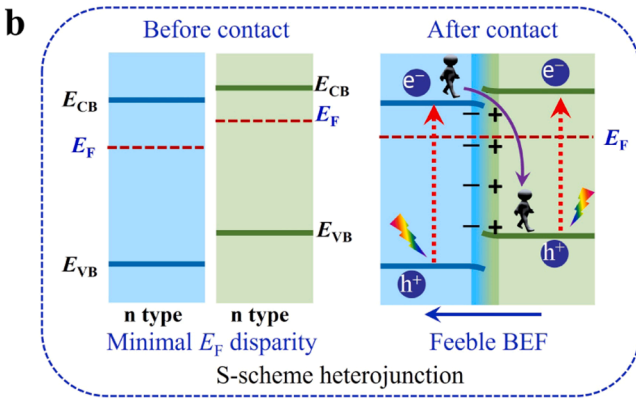
E-mail addresses: zm2016@email.tjut.edu.cn (M. Zhang), lutongbu@tjut.edu.cn (T.-B. Lu).

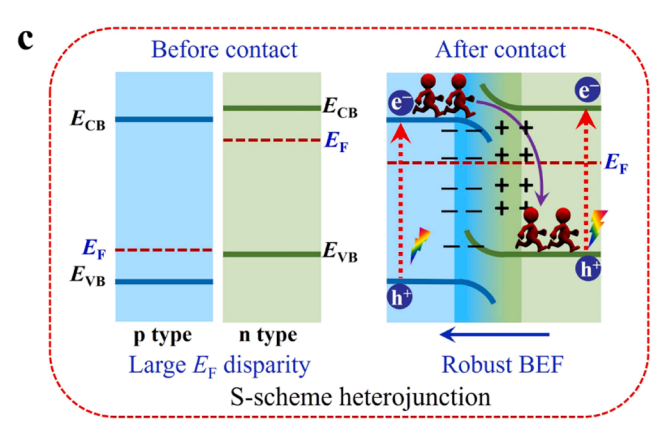
^a MOE International Joint Laboratory of Materials Microstructure, Institute for New Energy Materials and Low Carbon Technologies, School of Materials Science and Engineering, Tianjin University of Technology, Tianjin 300384, China

b School of Chemistry and Chemical Engineering, Yangzhou University, Yangzhou, Jiangsu 225009, China

^{*} Corresponding authors.







Scheme 1. Schematic of built-in electric field (BEF) formation and interfacial photogenerated electrons transfer within (a) type-II heterojunction and S-scheme heterojunctions composed of (b) the same type (e.g., n-type) and (c) different type of semiconductors.

(Scheme 1a) or S-scheme [32] (Scheme 1b) pathway, depending on the relative positions of their Fermi levels. Compared to Type-II heterojunctions, S-scheme heterojunctions not only facilitate the separation of photogenerated carriers, but also maintain high redox potentials [33–35], which is crucial for HPs due to their weak water oxidation capacity [36,37]. Nevertheless, the currently reported HP-based S-scheme heterojunctions consist of two n-type semiconductors (Scheme 1b). The minimal disparity in their Fermi levels gives rise to a feeble built-in electric field (BEF), hindering the sufficient separation of photogenerated carriers. Combining HPs with suitable p-type semiconductors to form S-scheme heterojunctions (Scheme 1c), and leveraging the substantial disparity in their Fermi levels to generate a robust BEF, is expected to further facilitate charge separation and enhance their photocatalytic CO_2 reduction performance.

To demonstrate this concept, we fabricated a p-n heterojunction of

CABB/Co₃O₄ by in-situ growth of the n-type lead-free perovskite Cs₂AgBiBr₆ (CABB) onto the surface of p-type porous Co₃O₄, and employed it as a catalyst to achieve CO2 photoreduction with H2O as the electron donor. As a typical water oxidation catalyst, p-type Co₃O₄ exhibits a Fermi level notably different from that of the n-type CABB [38, 39], leading to the creation of a robust BEF at the heterojunction interface, which facilitates the spatial separation of photogenerated carriers adhering to the S-scheme charge transfer mechanism. Additionally, the BEF intensity was further enhanced by passivating the CABB defect with Na doping to improve its carrier mobility. As anticipated, the electrons consumption rate of the Na-CABB/Co₃O₄ heterojunction reached up to 1336 µmol g⁻¹ h⁻¹ for converting CO₂ into CO and CH₄ using H₂O as the electron donor, setting a record-high value among the reported HP-based materials without the need for sacrificial agents (Table S1). Furthermore, the mechanisms underlying photogenerated carrier separation and CO₂ photoreduction were comprehensively elucidated through photophysical characterizations, in-situ diffuse reflectance infrared Fourier transform spectroscopy (DRIFTS) measurements, and density functional theory (DFT) calculations.

2. Experimental procedures

2.1. Materials

Cobalt nitrate hexahydrate (Co(NO₃)₂·6H₂O) and sodium hydroxide (NaOH) were purchased from Fu Chen. Cesium bromide (CsBr, 99.5 %) was purchased from Xi'an Polymer Light Technology Corp. Hydrogen bromide (HBr, 48 wt% in water) and bismuth bromide (BiBr₃ ≥ 98 %) were purchased from Acros. 2-Methylimidazole, styrene (99.5 %), anhydrous methanol (CH₃OH, HPLC, 99.5 %), ammonia solution (NH $_3$ ·H $_2$ O, 25.0–30.0 wt%), potassium persulfate (K $_2$ S $_2$ O $_8$, 99 %), potassium bromide (KBr, SP, \geq 99.5 %), sodium bromide (NaBr, \geq 99 %), isopropanol (\geq 99.5 %), N,N-dimethyl formamide (DMF, HPLC, \geq 99.9 %), dimethyl sulfoxide (DMSO, \geq 99.5 %), and acetonitrile (HPLC, > 99.9 %) were purchased from Innochem. Silver nitrate (AgNO₃) was purchased from GENERAL-REAGENT. Nitric acid (HNO3, 68 %) was purchased from China National Pharmaceutical Group Corporation. Tetrabutylammonium hexafluorophosphate (TBAPF₆, 98 %) was purchased from Aladdin. Carbon dioxide (CO_2 , ≥ 99.999 %), nitrogen (N_2 , 99.999 %), and argon (Ar, \geq 99.999 %) were purchased from Tianjin Huanyu Gas Co., Ltd. 13CO2 and H28O were purchased from Energy Chemical. Ultrapure water with a resistivity of 18.2 M Ω ·cm was sourced from Milli-O water purification system

2.2. Sample preparation

Synthesis of polystyrene (PS) spheres template. In a typical synthesis [40], 0.083 g of K₂S₂O₈ was dissolved in 12.5 mL of ultrapure water within a 25 mL flask and subsequently heated to 70 °C. Concurrently, 212.5 mL of ultrapure water was added to a 500 mL three-necked flask, degassed with nitrogen for 30 minutes, and then heated to 70 °C. Once the temperature stabilized, 22.2 mL of styrene, which had been washed four times with 0.1 M NaOH solution and then with ultrapure water, respectively, was carefully added to the flask. After ensuring temperature stability, the prepared K₂S₂O₈ solution was gently poured into the styrene mixture, which was then maintained at this temperature for 28 hours under stirring at 360 rpm. It is crucial to maintain a low stirring speed during the polymerization process, as excessive rotation can promote agglomeration of the PS template. Upon completion of the reaction and natural cooling, the resulting turbid solution underwent centrifugation at 2000 rpm for 6 hours to separate the supernatant. The resulting precipitate was then vacuum-dried at 60 °C overnight to yield the final PS microsphere template.

Synthesis of PS@ZIF-67. 0.50 g of PS sphere template was immersed in 50 mL of a methanol solution containing 7.85 g of $Co(NO_3)_2$ -6 $Co(NO_3)_2$ -7 $Co(NO_3)_2$ -8 $Co(NO_3)_2$ -8 Co(NO

infiltration of the precursor solution into the voids of the template [41]. The resulting turbid mixture was centrifuged at 3000 rpm to obtain precipitate (PS@precursor), which was then dried at 65 °C overnight. Subsequently, the PS@precursor was transferred into a 50 mL mixture of NH $_3$ ·H $_2$ O and CH $_3$ OH (V:V=1:1) to initiate the formation of zeolitic imidazolate frameworks (ZIF-67). After a 24-hour immersion period, the PS@ZIF-67 composite was harvested via centrifugation at 3000 rpm and further dried at 65 °C for subsequent applications.

Synthesis of porous Co_3O_4 . The PS@ZIF-67 composite was thoroughly washed three times using DMF solvent to ensure complete removal of the PS template. Following this, the ZIF-67 material was subjected to annealing in an air atmosphere at 450 °C for 3 hours with a heating rate of 2 °C per minute. This thermal treatment ultimately led to the formation of porous Co_3O_4 .

Synthesis of CABB and Na-CABB nanocrystals. CABB was synthesized by modifying our previously reported antisolvent methods [39]. Briefly, AgBr was prepared by reacting HBr and AgNO₃ at room temperature. Then, 45 mg of AgBr, 110 mg of CsBr, and 112 mg of BiBr₃ were dissolved in 5 mL of an HBr solution. The mixture was heated to 110 °C with stirring under closed conditions for 2 hours, and then cooled to room temperature, followed by keeping unperturbed for 1 hour to generate orange precipitation. Subsequently, the prepared precipitate was washed with ethanol three times, and then a certain amount of the dried precipitate was dissolved in 4 mL of DMSO solvent. Finally, CABB nanocrystals were obtained by adding 40 mL of isopropanol (as the antisolvent) to the DMSO solution, followed by centrifugation and washing with ethanol. Na-CABB was prepared under exactly the same conditions as CABB, except that 2 mg of NaBr was added.

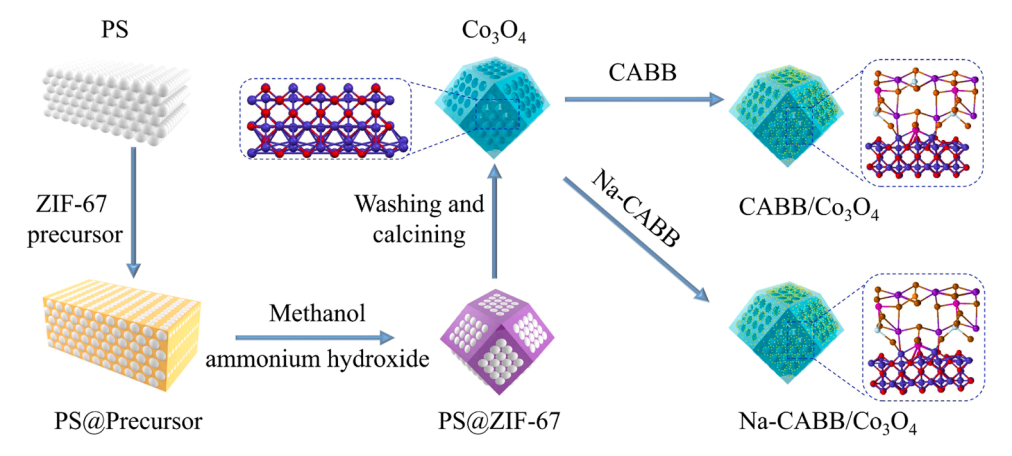
Synthesis of CABB/Co₃O₄ and Na-CABB/Co₃O₄ composites. 10 mg of as-prepared CABB or Na-CABB nanocrystals were dissolved in 1 mL of DMSO solvent, and the resulting mixture was then sonicated until complete dissolution to produce the perovskite precursor solution. In parallel, 5 mg of porous ${\rm Co_3O_4}$ was dispersed in 1 mL of DMSO solvent and sonicated for 30 minutes. Subsequently, the ${\rm Co_3O_4}$ dispersion was added to the previously prepared perovskite precursor solution. The combined mixture was then sonicated for an additional hour. Following this, the solution was stirred at 300 rpm for 10 hours. To obtain the CABB/Co₃O₄ and Na-CABB/Co₃O₄ composites, 40 mL of isopropanol as the antisolvent was added to the corresponding solutions, leading to the precipitation and deposition of CABB and Na-CABB on the pore walls of ${\rm Co_3O_4}$. Furthermore, CABB/Co₃O₄-5 and CABB/Co₃O₄-15 were also synthesized by adjusting the quantity of CABB used to 5 mg and 15 mg, respectively, while keeping all other synthesis conditions constant.

3. Results and discussion

3.1. Preparation and structure characterization

As illustrated in Scheme 2, both the CABB/Co₃O₄ and Na-CABB/ Co₃O₄ composites were synthesized through a straightforward procedure involving the in-situ growth of CABB and Na-CABB, within the pores of porous Co₃O₄, respectively. The detailed synthesis protocols are provided in the section of experimental procedures. Initially, polystyrene (PS) microspheres, obtained by a simple styrene polymerization method [40], served as three-dimensional (3D)-ordered templates. These templates were impregnated with a ZIF-67 precursor solution to form "PS@precursor" monoliths, which were subsequently transformed into PS@ZIF-67 through immersion in a mixed solvent of CH3OH and NH_3 : H_2O (V:V=1:1) [41]. The porous ZIF-67 was obtained by washing PS@ZIF-67 three times with N,N-dimethylformamide (DMF), and then annealing under an air atmosphere at 450 °C for 3 hours to generate porous Co₃O₄. Thereafter, CABB or Na-CABB nanocrystals and Co₃O₄ were dispersed in dimethyl sulfoxide solvent, respectively, and the two solutions were mixed. The mixture underwent sonication for 1 hour, followed by stirring at 300 rpm for 10 hours. Finally, CABB/Co₃O₄ or Na-CABB/Co₃O₄ composites were obtained through recrystallization by the addition of 40 mL of isopropanol.

The high-resolution scanning electron microscopy (HRSEM) measurements revealed that the as-prepared PS microspheres exhibit a regular spherical configuration with an average size of 400 nm (Fig. S1). The HRSEM image of the as-prepared ZIF-67 indicates the presence of abundant pores with a diameter of approximately 400 nm (Fig. S2), matching the size of the pure PS microspheres. This result indicates the complete removal of PS microspheres by DMF. Furthermore, porous Co₃O₄, derived from the transformation of ZIF-67, maintains its porosity with a slightly reduced diameter of approximately 395 nm (Fig. 1a and Fig. S3a). Energy-dispersive X-ray spectroscopy (EDS) mapping measurements (Figs. S3b and c) demonstrated the uniform distribution of O and Co elements. The HRSEM image of a typical CABB/Co₃O₄ composite also reveals a regular porous structure (Fig. 1b), indicating that the synthesis procedure of in situ growth preserves the parent morphology. Additionally, attached nanoparticles are clearly observed on its pore walls, and the pore diameter is reduced to around 350 nm (Fig. 1b), signifying that CABB nanocrystals were successfully grown within the pores of Co₃O₄, with a size of approximately 22 nm. For subsequent performance comparison, CABB nanocrystals were controlled at ~ 22 nm (Fig. S4). Moreover, the HRTEM image of CABB/Co₃O₄ (Fig. 1c) displays well-defined lattice spacings of 0.244 nm and 0.281 nm, which can be assigned to the (311) lattice plane of cubic phase Co₃O₄ and the (022) lattice plane of cubic phase CABB, respectively, further demonstrating the successful formation of CABB on the porous Co₃O₄ skeleton.



Scheme 2. Schematic illustration of the synthesis processes of CABB/Co₃O₄ and Na-CABB/Co₃O₄.

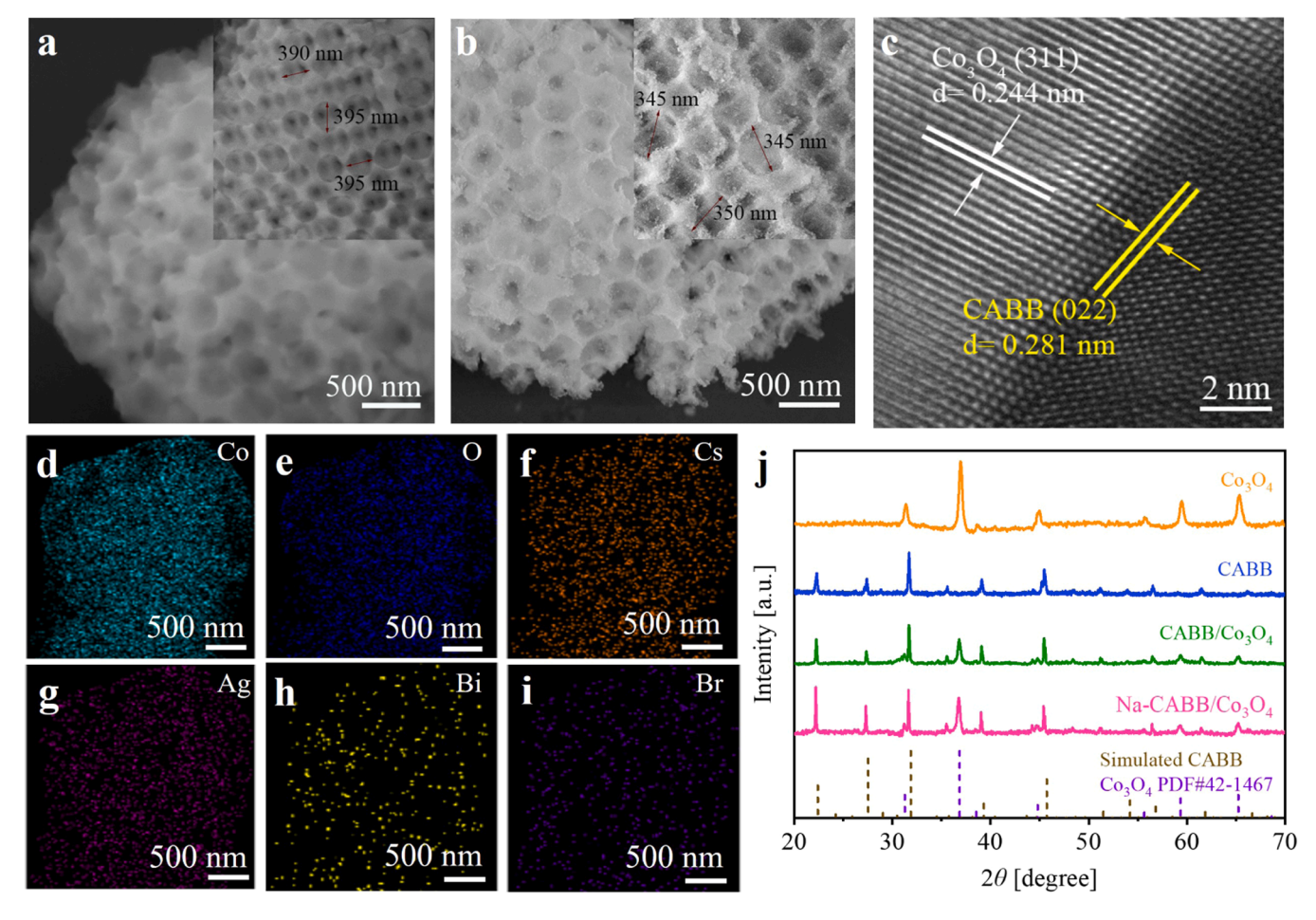


Fig. 1. HRSEM images of (a) Co_3O_4 and (b) $CABB/Co_3O_4$. (c) HRTEM image of $CABB/Co_3O_4$. (d-i) EDS elemental mapping images of $CABB/Co_3O_4$: (d) Co, (e) O, (f) Cs, (g) Ag, (h) Bi, and (i) Br. (j) XRD patterns of Co_3O_4 , CABB, $CABB/Co_3O_4$, and $Na-CABB/Co_3O_4$.

EDS mapping measurements also manifested that Co, O, Cs, Ag, Bi, and Br are uniformly distributed in the porous skeleton (Fig. 1d–i). Additionally, the HRSEM image of the Na-CABB/Co $_3$ O $_4$ composite also exhibits a porous structure (Fig. S5). The pore diameter within the Co $_3$ O $_4$ component of the composite is reduced to \sim 350 nm (Fig. S5a), signifying that Na-CABB nanocrystals were successfully grown within the pores of Co $_3$ O $_4$. EDS mapping measurements demonstrated the uniform distribution of Na, Cs, Ag, Bi, Br, Co, and O in the porous skeleton (Figs. S5b–h). Additionally, inductively coupled plasma mass spectrometry (ICP-MS) analysis (Fig. S6) revealed that the actual mass fraction of Na in Na-CABB nanocrystals is 0.14 %.

Powder X-ray diffraction (PXRD) measurements were employed to ulteriorly inspect the compositions of the as-prepared heterojunctions and their intermediates. As presented in Fig. S7, the XRD pattern of the pre-prepared PS microspheres reveals low crystallinity, displaying a broad and faint diffraction peak. Apart from the characteristic diffraction peak belonging to PS microspheres, distinct diffraction peaks consistent with the simulated pattern of ZIF-67 can also be clearly observed in the XRD pattern of PS@ZIF-67 (Fig S7), signifying the successful generation of ZIF-67 in the interstices of PS templates. After washing PS@ZIF-67 three times with DMF, the XRD pattern of the resulting ZIF-67 (Fig. S7) shows the complete disappearance of the diffraction peak corresponding to PS microspheres, further confirming the thorough removal of PS microspheres. Subsequent calcination of ZIF-67 under an air atmosphere results in an XRD pattern displaying distinct diffraction peaks consistent with the standard PDF card of the Fd-3m (227) cubic phase Co₃O₄, demonstrating the successful formation of well-crystallized Co₃O₄. By fitting the N₂ adsorption-desorption

isotherms of Co₃O₄ with the BET model, the BET surface area of porous Co_3O_4 can be calculated to be up to 17 m² g⁻¹ (Fig. S8). The abundance of pores in Co₃O₄ provides favorable conditions for the insitu growth of CABB or Na-CABB nanocrystals. As illustrated in Fig. 1j, the XRD patterns of CABB/Co₃O₄ and Na-CABB/Co₃O₄ unmistakably exhibit characteristic diffraction peaks corresponding to both Co₃O₄ and CABB, proving once again the successful in-situ growth of CABB and Na-CABB on the porous Co₃O₄. Additionally, Raman spectroscopy measurements provided further evidence confirming the successful preparation of the composites. As illustrated in Fig. S9, both the Raman spectra of CABB/Co₃O₄ and Na-CABB/Co₃O₄ exhibit the characteristic signal for CABB at 174.6 cm⁻¹, corresponding to the symmetric stretching vibration of $A_{1\,g}$ mode attributed to the Br atoms surrounding Bi atoms in the octahedron [42]. Furthermore, the prominent peak associated with the $A_{1\,g}$ mode of Co_3O_4 at 690 cm⁻¹ is also discernible in the Raman spectra of CABB/Co₃O₄ and Na-CABB/Co₃O₄ [5]. For comparative analysis, solo CABB and Na-CABB were also synthesized. As depicted in Fig. S10a, the CABB nanocrystals with Na doping consistently exhibit crystal features characteristic of the cubic phase CABB (ICSD: 230901), indicating the retention of the intrinsic structure of CABB after small amount of Na doping. Whereas Na doping brings forth slight shifts of XRD peaks towards lower 2θ angles, as evident in the (022) diffraction peak in Fig. S10b. This shift is attributed to the slightly longer bond length of Na-Br (2.841 Å) [43] compared to that of Ag-Br (2.822 Å) [44], leading to lattice expansion [45].

3.2. Interaction and charge transfer at the heterojunction interface

The energy band structures of Co₃O₄ and CABB were firstly inspected by UV-visible diffuse reflectance spectroscopy (UV-Vis DRS) and Mott-Schottky measurements, which play a vital role in determining the interfacial interaction and charge transfer of CABB/Co₃O₄. Based on the Tauc plots (the inserts in Fig. S11) derived from the UV-Vis DRS spectra (Fig. S11) [46], the band gaps (E_g) of Co₃O₄ and CABB can be calculated as 1.92 and 2.03 eV, respectively. The Mott-Schottky plots of Co₃O₄ and CABB (Fig. S12) show negative and positive slopes, respectively, thereby confirming the respective p-type and n-type behaviors of Co₃O₄ and CABB [47,48]. Consequently, the conduction band edge potential (E_{CB}) value of CABB and the valence band edge potential (EVB) value of Co₃O₄ can be roughly determined by their flat band potentials derived from corresponding Mott-Schottky plots, being -0.91 and 1.31 V versus the standard hydrogen electrode (vs. SHE, pH = 7, for which 0 V vs. SHE equals -4.44 eV vs. Vacuum level), respectively. In combination with the values of $E_{\rm S}$, the value of $E_{\rm VB}$ for CABB and the $E_{\rm CB}$ value for Co₃O₄ can be deduced to be 1.12 and -0.61 V vs. SHE, respectively. Based on the above results, the obtained energy band structures of Co₃O₄ and CABB exhibit a staggered band structure configuration as illustrated in Fig. 2a.

The ultraviolet photoelectrons spectroscopy (UPS) measurements were further carried out to analyze the difference in the Fermi energy levels ($E_{\rm F}$) of CABB and Co₃O₄, which determines the migration orientation of interfacial free electrons during the formation of CABB/Co₃O₄ heterojunction. As depicted in Fig. 2b and c, the work functions of CABB and Co₃O₄ are deduced to be 4.09 and 5.40 eV, respectively, indicating that Co₃O₄ has a significantly lower $E_{\rm F}$ (–5.40 eV ν s. vacuum) than CABB (–4.09 eV ν s. vacuum), as illustrated in Fig. 2a. To achieve $E_{\rm F}$ equilibrium in the heterojunction system, the significantly higher $E_{\rm F}$ of CABB relative to Co₃O₄ will result in the transfer of large amount of free electrons from CABB to Co₃O₄ when they are in close proximity, leading to the formation of energy band bending and a strong interfacial BEF

pointing from CABB to Co₃O₄ (Fig. 2d). The large Fermi level difference between CABB and Co₃O₄ can be further confirmed by DFT calculation. As depicted in Fig. 2e, there is a large surface electric potential difference of 14.9 eV within CABB/Co₃O₄, which is proportional to the Fermi level difference between CABB and Co₃O₄. The significantly enhanced intensity of the BEF at the interface of the CABB/Co₃O₄ heterojunction has been demonstrated by the surface voltage and surface accumulated electron density measurements (Fig. S13). Based on the model proposed by Kanata et al. [49,50], the calculated BEF intensity of CABB/Co₃O₄ is 5.7 and 3.5 times higher than that of Co₃O₄ and CABB, respectively (Fig. 2f). It is noted that the $E_{\rm F}$ of CABB was moved up by 0.08 eV (-4.01 eV) after doping by sodium (Fig. S14), which endows Na-CABB/Co₃O₄ with an increscent surface electric potential difference of 16.3 eV compared to CABB/Co₃O₄, as illustrated in Fig. S15. Notably, although Na doping only slightly elevates the Fermi energy level of CABB, it significantly enhances the intensity of the BEF at the interface of the Na-CABB/Co₃O₄ heterojunction (Fig. S13), which is 2.3 times higher than that of CABB/Co₃O₄ (Fig. 2f). This phenomenon may be attributed to the fact that the addition of Na⁺ ions can significantly diminish the defect density within CABB nanocrystals (Fig. S16a) as demonstrated in previous reports [51,52], which leads to a decreased likelihood of non-radiative recombination process (Fig. S16b) and enhances the mobility of charge carriers.

The free electron transfer between Co_3O_4 and CABB during the formation of heterojunction was further analyzed using X-ray photoelectron spectroscopy (XPS) measurements (Fig. S17). The binding energy shifts (Δ_{BE}) of the elements after CABB is loaded onto Co_3O_4 are summarized in Fig. 3a. Notably, the binding energies of Co 2p and O 1 s in CABB/ Co_3O_4 are evidently smaller than those of pure Co_3O_4 , with shifts of ~ 0.35 –0.40 eV for Co and ~ 0.20 eV for O. Meanwhile, compared to pristine CABB, all the peaks of Cs 3d, Ag 3d, Bi 4f, and Br 3d in CABB/ Co_3O_4 are noticeably shifted toward higher binding energy (Cs 3d: ~ 0.10 eV, Ag 3d: ~ 0.30 eV, Bi 4f: ~ 0.30 eV, Br 3d: ~ 0.15 eV). The

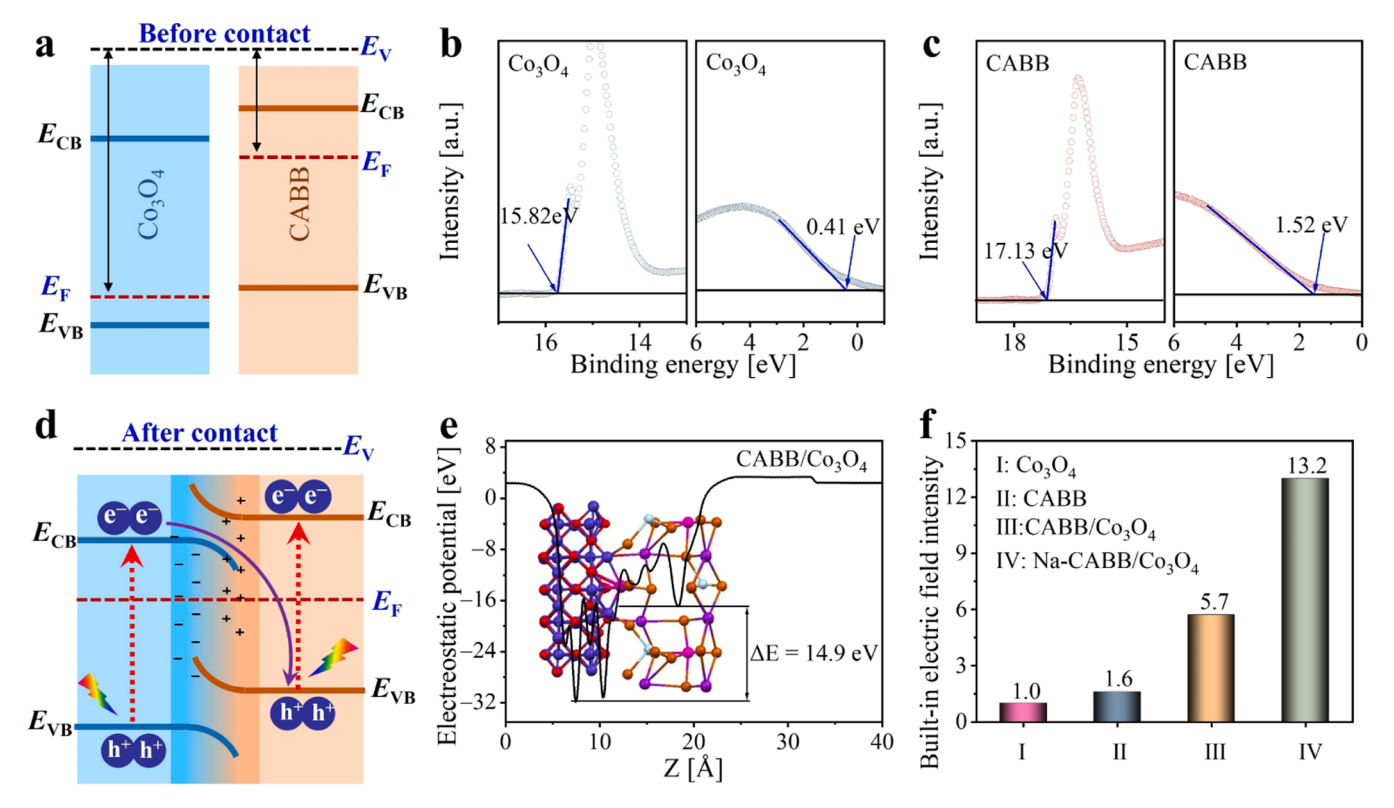


Fig. 2. (a) Energy band structures of CABB and Co_3O_4 . UPS spectra of (b) Co_3O_4 and (c) CABB. (d) The most conceivable photogenerated carrier transfer pathway in CABB/ Co_3O_4 heterojunction. (e) The calculated electrostatic potential difference for CABB/ Co_3O_4 (inset images: configuration of the CABB/ Co_3O_4 heterojunction). Z, the position along z axis. (f) The relative intensity of BEF of Co_3O_4 , CABB, CABB/ Co_3O_4 , Na-CABB/ Co_3O_4 .

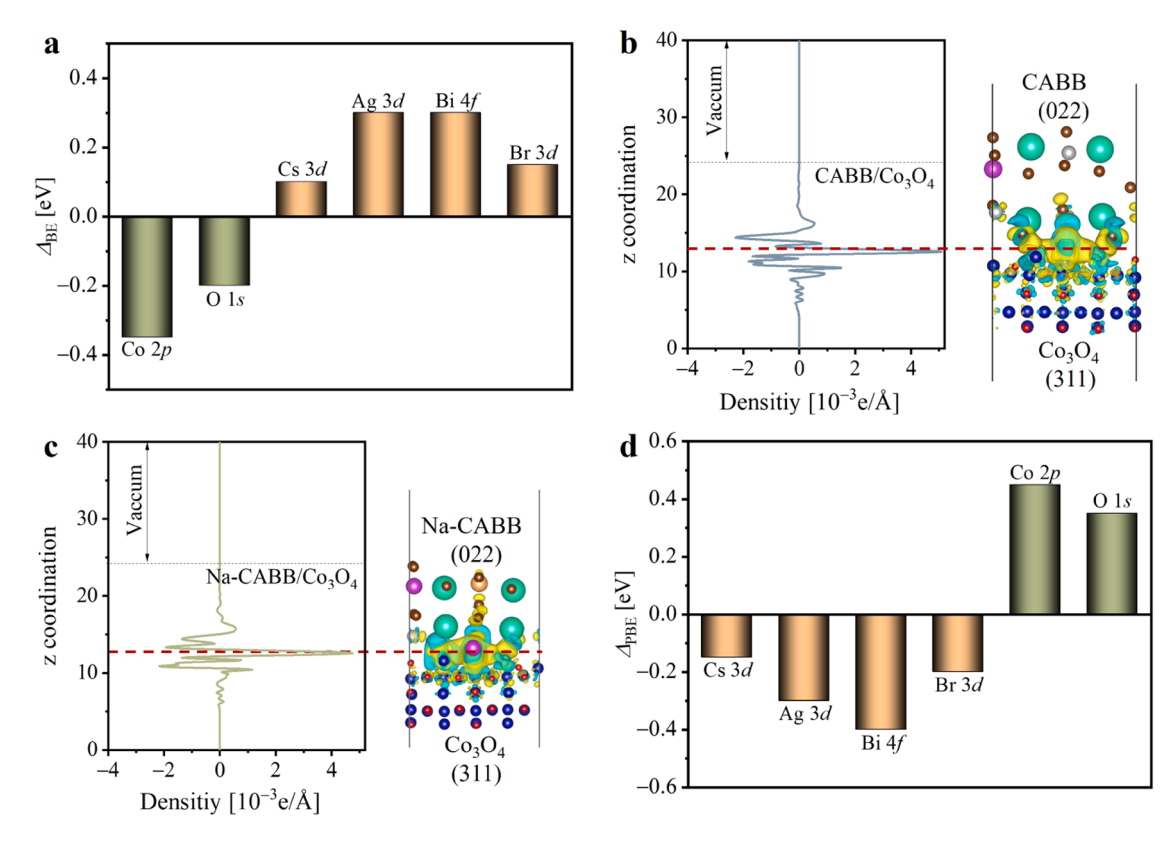


Fig. 3. (a) Binding energy shifts (Δ_{BE}) in CABB/Co₃O₄ compared to individual components under dark conditions. Schematic of calculated charge densities between CABB and Co₃O₄ (yellow: electron accumulation and cyan: electron depletion) for (b) CABB/Co₃O₄ and (c) Na-CABB/Co₃O₄. (d) Photoinduced binding energy shifts (Δ_{PBE}) in CABB/Co₃O₄ derived from ISI-XPS measurements under light illumination.

significant difference in element binding energy between CABB/Co₃O₄ and its separate ingredient signifies a strong electronic coupling at the interface of CABB/Co₃O₄, which can promote the interfacial transfer of photogenerated carriers. In addition, increases and decreases in binding energies generally represent a decrease and an increase, respectively, in the concentration of electrons around the nucleus. Therefore, the above XPS results indicate that free electron transfer from CABB to Co_3O_4 occurs during the formation of heterojunction between Co_3O_4 and CABB. This can be further demonstrated by analyzing the charge density difference at the interface of the CABB/Co₃O₄ heterojunction through DFT calculation. As depicted in Fig. 3b and c, there is obvious charge redistribution at the interfaces of both CABB/Co₃O₄ and Na-CABB/Co₃O₄. Evidently, charge consumption (cyan regions) occurs on CABB or Na-CABB side, while charge accumulation (yellow regions) is observed on the Co₃O₄ part.

In-situ irradiated XPS spectra were further recorded to monitor the changes of element binding energies upon light excitation (Fig. S18), thus unveiling the interfacial photogenerated charge transfer mode within CABB/Co₃O₄. The photoinduced binding energy shifts (Δ_{PBE}) of the elements within CABB/Co₃O₄ are summarized in Fig. 3d. It is noted that photoexcitation leads to a perceptible shift in the binding energies of Bi 4 f, Br 3d, Cs 3d, and Ag 3d in CABB/Co₃O₄ in the low-energy direction (0.15 \sim 0.40 eV). Meanwhile, both the peaks of Co 2p and O 1 s in CABB/Co₃O₄ are noticeably shifted toward higher binding energies $(0.35 \sim 0.45 \text{ eV})$ after light irradiation. These results demonstrate that photogenerated electrons and holes in CABB/Co₃O₄ accumulate in CABB and Co₃O₄, respectively. Therefore, the photogenerated carriers in the CABB/Co₃O₄ heterojunction should be separated by an S-scheme pathway, as illustrated in Fig. 2d. Specifically, the photogenerated electrons in the conduction band of Co₃O₄ are driven by the BEF to combine with the holes in the valence band of CABB, while the photogenerated holes in the valence band of Co₃O₄ and the photogenerated

electrons in the conduction band of CABB are retained. This interfacial charge transfer mode not only realizes the spatial separation of photogenerated electron-hole pairs, but also maintains the strong redox ability of photogenerated carriers. The efficient charge separation of the CABB/ Co_3O_4 heterojunction can be further evidenced by photoelectrochemical measurements. As presented in Fig. S19 and Table S2, CABB/Co $_3\text{O}_4$ exhibits a reduced charge transport resistance and an extended lifetime for photogenerated electrons compared to its individual components. Furthermore, the formation of a heterojunction using Na-doped CABB and Co_3O_4 can further amplify the interfacial charge separation efficiency, resulting in an even lower charge transport resistance and an even longer lifetime of photogenerated electrons relative to CABB/ Co_3O_4 .

3.3. Photocatalytic CO₂ reduction performance

The photoreduction activities of CO₂ for CABB/Co₃O₄ and Na-CABB/ Co₃O₄ were assessed in a gas-solid reaction apparatus in the presence of H₂O vapor (Fig. S20). For comparative analysis, standalone CABB and Co₃O₄ were also subjected to the same assessment conditions. Gas chromatography measurements revealed that the reduction products across all samples are primarily consisted of CO, accompanied by a small amount of CH₄ (Fig. S21), with no other reduction products detected. As evident in Fig. 4a, both CABB and Co₃O₄ exhibit low photocatalytic activity towards CO2 reduction. The CO yields of CABB and Co3O4 are only 32 and 45 μ mol g⁻¹ h⁻¹, respectively (Fig. 4b). The formation of the CABB/Co₃O₄ heterojunction leads to significantly enhanced performance for CO_2 photoreduction, boosting the yields of CO and CH_4 to 242 and $55 \,\mu\text{mol}\,g^{-1}\,h^{-1}$, respectively. This enhancement can be attributed to the efficient separation and preserved redox potentials of photogenerated carriers. Furthermore, as depicted in Table S3, CABB/Co₃O₄ exhibits optimal photocatalytic performance compared with CABB/

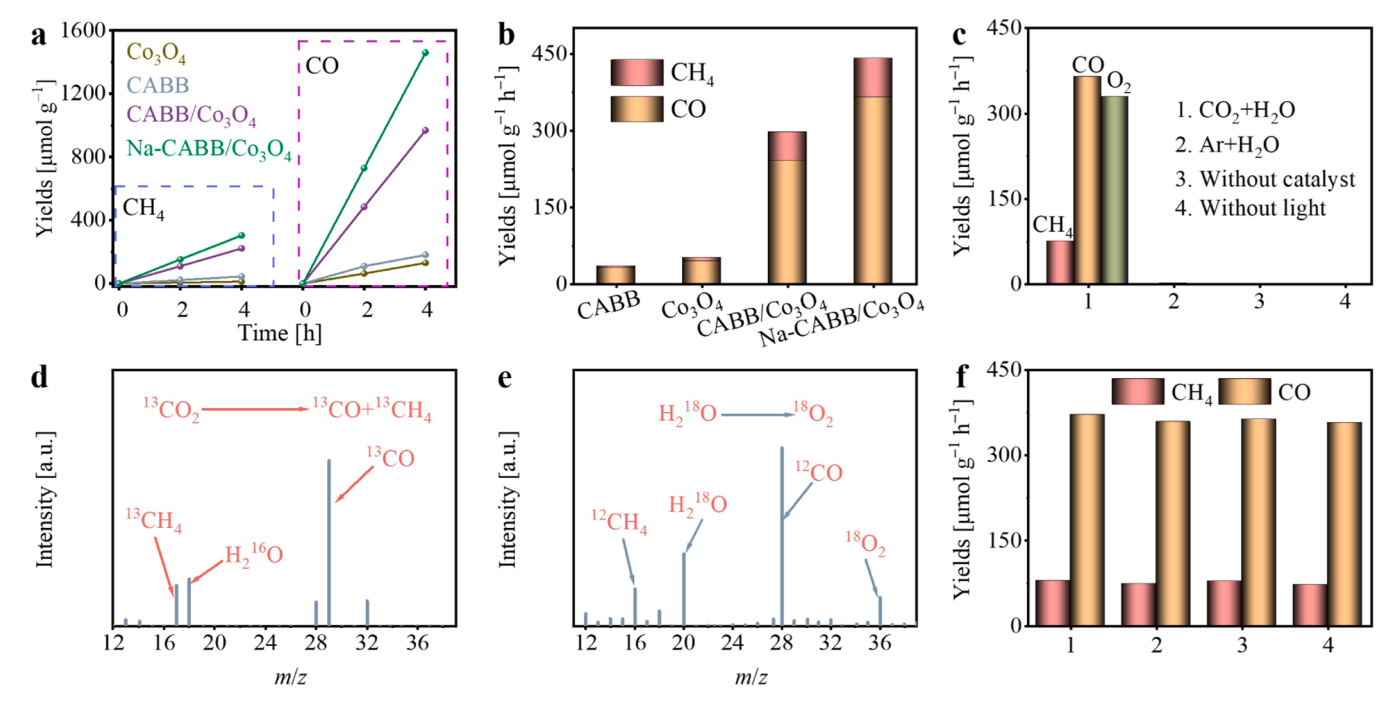


Fig. 4. (a, b) The yields of CO and CH₄ using Co₃O₄, CABB, CABB/Co₃O₄, and Na-CABB/Co₃O₄ as photocatalysts. (c) The yields of reduced and oxidized products with Na-CABB/Co₃O₄ as the photocatalyst. Mass spectra (MS) analyses for solar-driven reduction of (d) 13 CO₂ to 13 CO (m/z = 29) and 13 CH₄ (m/z = 17) and (e) H_2^{18} O to 18 O₂ (m/z = 36) using Na-CABB/Co₃O₄ as photocatalyst. (f) The stability test results of Na-CABB/Co₃O₄. The duration of each cycle is 4 h.

Co₃O₄-5 and CABB/Co₃O₄-15. Therefore, we investigated the influence of Na doping on catalytic performance, using the mass ratio of CABB and Co₃O₄ in the CABB/Co₃O₄ composite as an illustrative case. The integration of Co₃O₄ with Na-CABB brings forth even more impressive results, stemming from the strengthened interfacial BEF. The yields of CO and CH₄ for Na-CABB/Co₃O₄ reach up to 364 µmol g⁻¹ h⁻¹ and 76 µmol g⁻¹ h⁻¹, respectively. Notably, the corresponding electron consumption rate for CO₂ reduction reaches an impressive 1336 µmol g⁻¹ h⁻¹, surpassing individual CABB and Co₃O₄ by 15 and 8 times, respectively, and outperforming both lead-free and lead-based HP photocatalysts reported under comparable conditions so far (Table S1). Concurrently, the oxidation product O2 of Na-CABB/Co3O4 can also be detected with a yield of 334 μ mol g⁻¹ h⁻¹ (Fig. 4c), indicative of a good balance between photogenerated electron and hole consumption. It is noted that the selectivity of CH₄ has shown a slight improvement when using the composites of CABB and Co₃O₄ as photocatalysts (Table S3). This can be attributed to the efficient separation of photogenerated carriers at the heterojunction interface, resulting in a high concentration of photogenerated carriers, which facilitates the multi-electron reduction of CO₂ to CH₄ [53].

To elucidate the origins of the photocatalytic redox products, a comprehensive series of comparative experiments were undertaken, employing the Na-CABB/Co₃O₄ heterojunction as the photocatalyst. Absence of CO2, light or the catalyst individually results in nondetection of products (Fig. 4c), suggesting that CO and CH₄ originate from CO₂ photoreduction. This deduction can be further validated via a subsequent isotopic labeling experiment using ¹³CO₂, where distinct signals of m/z = 29 (attributed to ¹³CO) and m/z = 17 (corresponding to $^{13}\mathrm{CH_4})$ were clearly discernible in the corresponding mass spectrum (Fig. 4d). Meanwhile, utilizing H₂¹⁸O as the reactant shows a characteristic signal of $^{18}O_2$ at a m/z peak of 36 in the mass spectrum (Fig. 4e), confirming that the O2 was from H2O photooxidation. Furthermore, the photocatalytic stability of Na-CABB/Co₃O₄ was evaluated through cycling measurements. As presented in Fig. 4f, after undergoing four photocatalytic cycles, the decline in CO and CH4 generation rates was minimal, less than 10 %, demonstrating the good stability of Na-CABB/ Co₃O₄ in the gas-solid reaction system. Moreover, the XRD pattern

(Fig. S22), HRSEM image, (Fig. S23) and XPS spectra (Fig. S24) of Na-CABB/ Co_3O_4 exhibit negligible changes before and after the photocatalytic reaction, further attesting to the robust stability of Na-CABB/ Co_3O_4 for photocatalytic CO_2 reduction with water as the electron donor.

3.4. Photocatalytic mechanism of CO₂ reduction

Taking into account the separation of photogenerated carriers in the CABB/Co₃O₄ heterojunction through the S-scheme charge transfer route, where photogenerated electrons accumulate on CABB, DFT calculations were initially employed to analyze the density of states (DOS) of CABB, with the aim of uncovering its photocatalytic CO2 reduction active sites. According to the orbital-resolved projected DOS presented in Fig. 5a, the conduction band and valance band of CABB were mainly contributed by Bi 6p and Br 4p orbitals, respectively. Consequently, photogenerated electrons will accumulate on Bi atoms within CABB, which act as the active centers for photocatalytic CO2 reduction. This deduction can be further substantiated through in-situ irradiated XPS measurements, which can analyze the variations in the photoinduced binding energy of individual elements in CABB. As evident from Fig. 5b, upon light irradiation, a notable decrease in the binding energy of Bi 4 f within CABB is observed compared to its dark state. Conversely, the binding energy of Br 3d within CABB undergoes a noticeable shift toward higher energy upon switching from darkness to illumination, as depicted in Fig. 5c. Additionally, a slight increase in the binding energy of Ag 3d within CABB is also observed after illumination (Fig. 5d).

In-situ diffuse reflectance infrared Fourier transform spectroscopy (DRIFTS) measurements were further carried out to monitor the reaction intermediates during the photocatalytic CO₂ reduction process with CABB/CO₃O₄ as catalyst. As depicted in Fig. 6a, no discernible peaks are observed without light irradiation. However, upon illumination, distinct peaks emerge at 1270, 1355 and 1637 cm⁻¹, respectively, which are attributed to the stretching vibrations of O–H, C–O, and C=O in the *COOH intermediate groups [54]. This appearance of *COOH intermediate signals indicates that CO₂ is coordinated to the unsaturated Bi sites on the CABB/CO₃O₄ heterojunction surface via carbon atom [53]. The

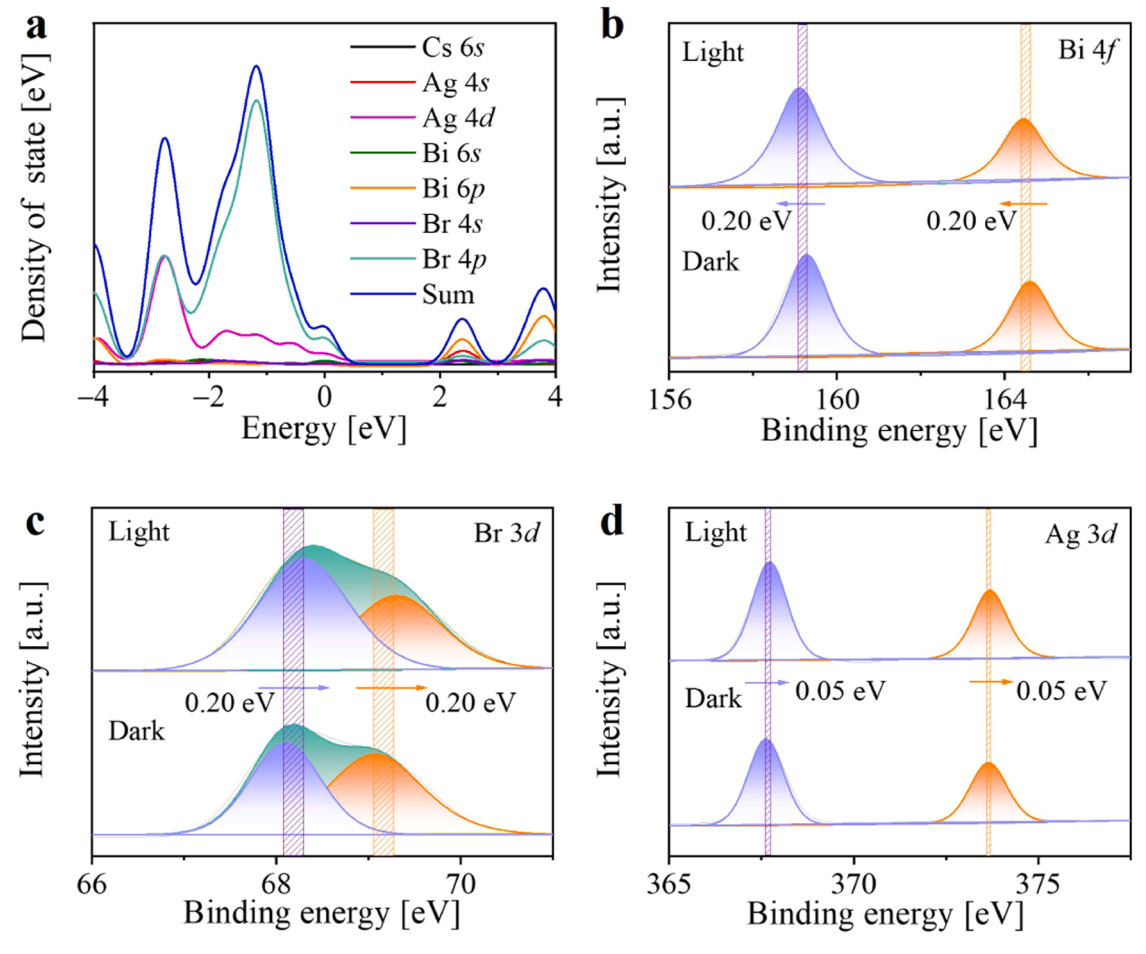


Fig. 5. (a) The density of states (DOS) of CABB. (b-d) High-resolution XPS of CABB/Co₃O₄: (b) Bi 4f, (c) Br 3d, and (d) Ag 3d.

characteristic peak at $1303~\rm cm^{-1}$ corresponds to the CO_3^{2-} intermediate. Furthermore, a characteristic peak at $2078~\rm cm^{-1}$ corresponds to the *CO intermediate [55]. CO is directly generated through the desorption of *CO, while the remaining *CO subsequently undergoes gradual hydrogenation and dehydration to form CH_4 , as illustrated in Fig. S25. The corresponding important intermediates *CHO, *CH₂O, and *CH₃O for the formation of CH_4 can also be detected, located at $1098~\rm cm^{-1}$, $1212~\rm cm^{-1}$, and $1058~\rm cm^{-1}$, respectively [53,56–58].

Furthermore, DFT calculations were performed to obtain the Gibbs free energies (ΔG) of several reaction intermediates. As depicted in Fig. 6b, upon adsorption on the Bi site, CO₂ is activated to form *CO₂ species. The ΔG values for the *COOH intermediates, generated via the protonation of *CO₂ species, are determined to be 0.69 and 0.53 eV for CABB/Co₃O₄ and Na-CABB/Co₃O₄, respectively. This manifests that the first electron-transfer process is the rate-limiting step for CO₂ photoreduction when using either CABB/Co₃O₄ or Na-CABB/Co₃O₄ as the photocatalyst [59–61]. The energy barrier in the rate-limiting step of the Na-CABB/Co₃O₄ is distinctly lower than that of CABB/Co₃O₄, which can be attributed to the enhanced interaction between CABB and CO2 within the Na-CABB/Co₃O₄ heterojunction. Subsequently, the *CO intermediate can be acquired through a sequential process of protonation and dehydration of the *COOH species. Notably, the lower ΔG for *CO desorption compared to that for *CHO formation from *CO hydrogenation indicates that CO is the main product of CO₂ photoreduction. Meanwhile, the minor fraction of undesorbed *CO subsequently undergoes hydrogenation to form CH4.

4. Conclusion

In summary, we have successfully prepared a p-n type heterojunction of CABB/Co₃O₄ by combining the n-type lead-free perovskite CABB with the p-type porous Co₃O₄ through a facile in-situ growth strategy, which demonstrates excellent photocatalytic performance for CO2 reduction coupled with H₂O oxidation. The substantial difference in Fermi level between CABB and Co₃O₄ endows the CABB/Co₃O₄ heterojunction with a robust BEF, which facilitates efficient photocarrier separation following an S-scheme transfer mechanism as evidenced by photoelectrochemical measurements, ISI-XPS analyses and DFT calculations. In addition, the introduction of Na ions into CABB can further strengthen the BEF and facilitate CO₂ adsorption and activation. Consequently, the p-n heterojunction Na-CABB/Co₃O₄ exhibits unprecedented performance for the overall reaction of artificial photosynthesis, achieving an electron consumption rate of 1336 µmol g⁻¹ h⁻¹ for CO₂ photoreduction. The strategy of leveraging significant disparities in Fermi levels to intensify the BEF and thereby ameliorate charge separation could be extended to photocatalysts utilizing other semiconductors, opening up a new avenue for enhancing the performance of photocatalysis.

CRediT authorship contribution statement

Zhao-Lei Liu: Methodology, Investigation, Writing – original draft. Yan-Fei Mu: Methodology. Xi-Rui Li: Methodology. You-Xiang Feng: Methodology. Min Zhang: Conceptualization, Methodology, Writing – review & editing, Funding acquisition, Resources, Supervision. Tong-Bu Lu: Funding acquisition, Resources, Supervision.

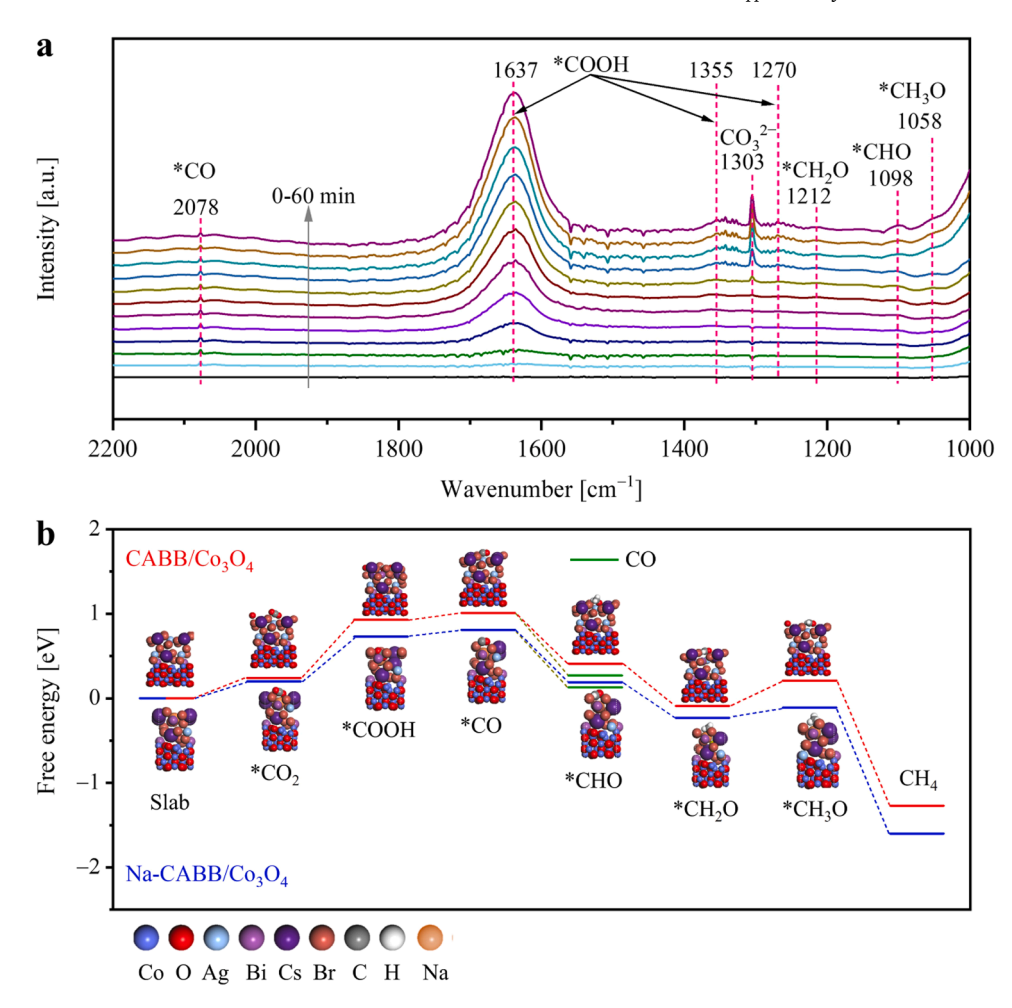


Fig. 6. (a) In-situ DRIFTS spectra of intermediates recorded at different reaction times with the CABB/ Co_3O_4 as the photocatalyst. (b) Gibbs free energy pathway of CABB/ Co_3O_4 and Na-CABB/ Co_3O_4 for photocatalytic CO_2 reduction.

Declaration of Competing Interest

The authors declare that they have no known competing financial interests or personal relationships that could have appeared to influence the work reported in this paper.

Acknowledgments

This work was financially supported by National Key Research and Development Program of China (2022YFA1502902), NSFC (22475152, U21A20286 and 22305214), and the 111 Project of China.

Appendix A. Supporting information

Supplementary data associated with this article can be found in the online version at doi:10.1016/j.apcatb.2024.125012.

Data Availability

Data will be made available on request.

References

- [1] J. Lv, J. Xie, A.G.A. Mohamed, X. Zhang, Y. Feng, L. Jiao, E. Zhou, D. Yuan, Y. Wang, Solar utilization beyond photosynthesis, Nat. Rev. Chem. 7 (2023) 91–105.
- [2] Y. Wang, H. He, Y. Li, W. Wang, L. Deng, L. Wu, Y. Zhang, J. Huang, P. Zhang, G. Yu, Y.-N. Liu, Unraveling the photo-induced dynamic behavior of COF-based Z-scheme heterostructure monolithic aerogels, Matter 7 (2024) 3145–3162.

- [3] K.K. Sakimoto, A.B. Wong, P. Yang, Self-photosensitization of nonphotosynthetic bacteria for solar-to-chemical production, Science 351 (2016) 74–77.
- [4] M. Rahaman, V. Andrei, D. Wright, E. Lam, C. Pornrungroj, S. Bhattacharjee, C. M. Pichler, H.F. Greer, J.J. Baumberg, E. Reisner, Solar-driven liquid multi-carbon fuel production using a standalone perovskite–BiVO₄ artificial leaf, Nat. Energy 8 (2023) 629–638.
- [5] L. Wang, J. Wan, Y. Zhao, N. Yang, D. Wang, Hollow multi-shelled structures of Co₃O₄ dodecahedron with unique crystal orientation for enhanced photocatalytic CO₂ reduction, J. Am. Chem. Soc. 14 (2019) 2238–2241.
 [6] H. Huang, J. Zhao, H. Guo, B. Wang, H. Zhang, R.A. Saha, M. Zhang, F. Lai,
- [6] H. Huang, J. Zhao, H. Guo, B. Wang, H. Zhang, R.A. Saha, M. Zhang, F. Lai, Y. Zhou, R.-Z. Juan, P.-P. Chen, S. Wang, J.A. Steele, F. Zhong, T. Liu, J. Hofkens, Y.-M. Zheng, J. Long, M.B.J. Roeffaers, Noble-metal-free high-entropy alloy nanoparticles for efficient solar-driven photocatalytic CO₂ reduction, Adv. Mater. 36 (2024) 2313209.
- [7] Y. Xie, M. Wang, Q. Huang, Q. Huang, B. Shen, W. Song, H. Sheng, J. Zhao, A floatable photocatalyst to synergistically promote CO₂ reduction and water oxidation by creating oriented charge separation across a tri-phase interface, Energy Environ. Sci. 17 (2024) 4735–4745.
- [8] Q. Wang, L. Dong, M. Li, H. Lu, G. Wei, Y. Qu, G. Wang, Z-scheme heterojunction photocatalyst based on lanthanum single-atom anchored on black phosphorus for regulating surface active sites, therefore enhancing photocatalytic CO₂ reduction with ≈100% CO selectivity, Adv. Funct. Mater. 32 (2022) 2207330.
- [9] Y.A. Wu, I. McNulty, C. Liu, K.C. Lau, Q. Liu, A.P. Paulikas, C.-J. Sun, Z. Cai, J. R. Guest, Y. Ren, V. Stamenkovic, L.A. Curtiss, Y. Liu, T. Rajh, Facet-dependent active sites of a single Cu₂O particle photocatalyst for CO₂ reduction to methanol, Nat. Energy 4 (2019) 957–968.
- [10] Z. Luo, X. Ye, S. Zhang, S. Xue, C. Yang, Y. Hou, W. Xing, R. Yu, J. Sun, Z. Yu, X. Wang, Unveiling the charge transfer dynamics steered by built-in electric fields in BiOBr photocatalysts, Nat. Commun. 13 (2022) 2230.
- [11] Y. Meng, Y. Wu, Z. Liu, Creating electron traps in BiOBr nanosheet arrays by bulkphase F doping to restrain carrier recombination for efficient photoelectrochemical water splitting system, Appl. Surf. Sci. 677 (2024) 161062.
- [12] S. Hu, P. Qiao, X. Yi, Y. Lei, H. Hu, J. Ye, D. Wang, Selective photocatalytic reduction of CO₂ to CO mediated by silver single atoms anchored on tubular carbon nitride, Angew. Chem. Int. Ed. 62 (2023) e202304585.

- [13] B. Su, Y. Kong, S. Wang, S. Zuo, W. Lin, Y. Fang, Y. Hou, G. Zhang, H. Zhang, X. Wang, Hydroxyl-bonded Ru on metallic tin surface catalyzing CO₂ reduction with H₂O by infrared light, J. Am. Chem. Soc. 145 (2023) 27415–27423.
- [14] W. Soontornchaiyakul, S. Yoshino, T. Kanazawa, R. Haruki, D. Fan, S. Nozawa, Y. Yamaguchi, A. Kudo, CH₄ synthesis from CO₂ and H₂O of an electron source over Rh–Ru cocatalysts loaded on NaTaO₃: Sr photocatalysts, J. Am. Chem. Soc. 145 (2023) 20485–20491.
- [15] K. Kosugi, C. Akatsuka, H. Iwami, M. Kondo, S. Massaoka, Iron-complex-based supramolecular framework catalyst for visible-light-driven CO₂ reduction, J. Am. Chem. Soc. 145 (2023) 10451–10457.
- [16] W. Lyu, Y. Liu, J. Zhou, D. Chen, X. Zhao, R. Fang, F. Wang, Y. Li, Modulating the reaction configuration by breaking the structural symmetry of active sites for efficient photocatalytic reduction of low-concentration CO₂, Angew. Chem. Int. Ed. 62 (2023) e202310733.
- [17] Q. Zhang, S. Gao, Y. Guo, H. Wang, J. Wei, X. Su, H. Zhang, Z. Liu, J. Wang, Designing covalent organic frameworks with Co-O₄ atomic sites for efficient CO₂ photoreduction, Nat. Commun. 14 (2023) 1147.
- [18] P. Dong, X. Xu, R. Luo, S. Yuan, J. Zhou, J. Lei, Postsynthetic annulation of threedimensional covalent organic frameworks for boosting CO₂ photoreduction, J. Am. Chem. Soc. 145 (2023) 15473–15481.
- [19] M.V. Kovalenko, L. Protesescu, M.I. Bodnarchuk, Properties and potential optoelectronic applications of lead halide perovskite nanocrystals, Science 358 (2017) 745–750.
- [20] J. He, X. Wang, P. Feng, Y. Zhou, K. Wang, B. Zou, M. Zhu, Isostructural phase transition-induced piezoelectricity in all-inorganic perovskite CsPbBr₃ for catalytic CO₂ reduction, Appl. Catal. B-Environ. Energy 355 (2024) 124186.
- [21] Z.-Y. Chen, N.-Y. Huang, Q. Xu, Metal halide perovskite materials in photocatalysis: Design strategies and applications, Coord. Chem. Rev. 481 (2023) 215031.
- [22] J.-S. Zhao, Y.-F. Mu, L.-Y. Wu, Z.-M. Luo, L. Velasco, M. Sauvan, D. Moonshiram, J.-W. Wang, M. Zhang, T.-B. Lu, Directed electron delivery from a Pb-Free halide perovskite to a Co(II) molecular catalyst boosts CO₂ photoreduction coupled with water oxidation, Angew. Chem. Int. Ed. 63 (2024) e202401344.
- [23] X. Wang, J. He, X. Chen, B. Ma, M. Zhu, Metal halide perovskites for photocatalytic CO₂ reduction: An overview and prospects, Coord. Chem. Rev. 482 (2023) 215076.
- [24] T. Liu, F. Gao, Molecule additive design for perovskite light-emitting diodes operated at high current densities, Chem 9 (2023) 2058–2059.
- [25] D. Hansora, J.W. Yoo, R. Mehrotra, W.J. Byun, D. Lim, Y.K. Kim, E. Noh, H. Lim, J.-W. Jang, S. II Seok, J.S. Lee, All-perovskite-based unassisted photoelectrochemical water splitting system for efficient, stable and scalable solar hydrogen production, Nat. Energy 9 (2024) 272–284.
- [26] H. Fu, Q. Zhang, Y. Liu, Z. Zheng, H. Cheng, B. Huang, P. Wang, Photocatalytic overall water splitting with a solar-to-hydrogen conversion efficiency exceeding 2% through halide perovskite, Angew. Chem. Int. Ed. 63 (2024) e202411016.
- [27] J. Zhou, B. Gao, D. Wu, C. Tian, H. Ran, W. Chen, Q. Huang, W. Zhang, F. Qi, N. Zhang, Y. Pu, J. Qiu, Z. Hu, J. Du, Z. Liu, Y. Leng, X. Tang, Enhanced photocatalytic activity of lead-free Cs₂TeBr₆/g-C₃N₄ heterojunction photocatalyst and its mechanism, Adv. Fun. Mater. 139 (2017) 3513–3521.
- [28] Z.-L. Liu, H.-Y. Luo, M.-R. Zhang, Y.-F. Mu, F.-Q. Bai, M. Zhang, T.-B. Lu, The simultaneous improvement of redox capacity for lead-free Cs₂Sb₂Br₂-based photocatalyst to promote photocatalytic N₂ fixation, Chem. Eng. J. 491 (2024) 151913.
- [29] K. Su, S.-X. Yuan, L.-Y. Wu, Z.-L. Liu, M. Zhang, T.-B. Lu, Nanoscale Janus Z-scheme heterojunction for boosting artificial photosynthesis, Small 19 (2023) 2301192.
- [30] Y.-X. Feng, K. Su, Z.-L. Liu, S.-X. Yuan, Y.-F. Mu, M. Zhang, T.-B. Lu, A halide perovskite based ternary heterojunction with multi-shell hollow structure for stable and efficient artificial photosynthesis, Appl. Catal. B-Environ. Energy 347 (2024) 123821.
- [31] N. Li, X. Chen, J. Wang, X. Liang, L. Ma, X. Jing, D.-L. Chen, Z. Li, ZnSe nanorods–CsSnCl₃ perovskite heterojunction composite for photocatalytic CO₂ reduction, ACS Nano 16 (2022) 3332–3340.
- [32] W. Song, K.C. Chong, G. Qi, Y. Xiao, G. Chen, B. Li, Y. Tang, X. Zhang, Y. Yao, Z. Lin, Z. Zou, B. Liu, Unraveling the transformation from type-II to Z-scheme in perovskite-based heterostructures for enhanced photocatalytic CO₂ reduction, J. Am. Chem. Soc. 146 (2024) 3303–3314.
- [33] H. Huang, D. Verhaeghe, B. Weng, B. Ghosh, H. Zhang, J. Hofkens, J.A. Steele, M.B. J. Roeffaers, Metal halide perovskite based heterojunction photocatalysts, Angew. Chem. Int. Ed. 61 (2022) e202203261.
- [34] Y. Xi, Y. Xiang, T. Bao, Z. Li, C. Zhang, L. Yuan, J. Li, Y. Bi, C. Yu, C. Liu, Nanoarchitectonics of S-scheme heterojunction photocatalysts: a nanohouse design improves photocatalytic nitrate reduction to ammonia performance, Angew. Chem. Int. Ed. 63 (2024) e202409163.
- [35] X. Jiang, Z. Chen, Y. Shu, A.M. Idris, S. Li, B. Peng, J. Wang, Z. Li, In-situ assembled S-scheme heterojunction of CsPbBr₃ nanocrystals and W₁₈O₄₉ ultrathin nanowires for enhanced bifunctional photocatalysis, Appl. Catal. B-Environ. Energy 348 (2024) 123840.
- [36] Y.-F. Mu, H.-L. Liu, M.-R. Zhang, H.-J. Wang, M. Zhang, T.-B. Lu, Ligand-free CsPbBr₃ with calliandra-like nanostructure for efficient artificial photosynthesis, J. Energy Chem. 77 (2023) 317–325.
- [37] R. Das, A. Patra, S.K. Dutta, S. Shyamal, N. Pradhan, Facets-directed epitaxially grown lead halide perovskite-sulfobromide nanocrystal heterostructures and their improved photocatalytic activity, J. Am. Chem. Soc. 144 (2022) 18629–18641.

- [38] L. Nowakowski, C. Hudu, F. Zasada, J. Gryboś, W. Piskorz, A. Wach, Y. Kayser, J. Szlachetko, Z. Sojka, N₂O decomposition on singly and doubly (K and Li)-doped Co₃O₄ nanocubes-establishing key factors governing redox behavior of catalysts, J. Am. Chem. Soc. 146 (2024) 24450–24466.
- [39] Z.-L. Liu, M.-R. Zhang, G.-X. Dong, M. Zhang, T.-B. Lu, Highly selective photosynthesis of formic acid by unifying the products of CO₂ reduction and methanol oxidation, Sol. RRL 7 (2023) 2300300.
- [40] K. Shen, L. Zhang, X. Chen, L. Liu, D. Zhang, Y. Han, J. Chen, J. Long, R. Luque, Y. Li, B. Chen, Ordered macro-microporous metalorganic framework single crystals, Science 359 (2018) 206–210.
- [41] Y. Wang, G. Fan, S. Wang, Y. Li, Y. Guo, D. Luan, X. Gu, X.W. Lou, Implanting CoOx clusters on ordered macroporous ZnO nanoreactors for efficient CO₂ photoreduction, Adv. Mater. 34 (2022) 2204865.
- [42] S. Yoon, B. Fett, A. Frebel, S. Kroisl, B. Herbig, M. Widenmeyer, B. Balke, G. Sextl, K. Mandel, A. Weidenkaff, Sb-substituted Cs₂AgBiBr₆—as much as it could be?—influence of synthesis methods on Sb-substitution level in Cs₂AgBiBr₆, Energy Technol. 10 (2022) 2200197.
- [43] S. Zhao, K. Yamamoto, S. Iikubo, S. Hayase, T. Ma, First-principles study of electronic and optical properties of lead-free double perovskites Cs₂NaBX₆ (B = Sb, Bi; X = Cl, Br, I), J. Phys. Chem. Solids 117 (2018) 117–121.
- [44] E.T. McClure, M.R. Ball, W. Windl, P.M. Woodward, Cs₂AgBiX₆ (X = Br, Cl): New visible light absorbing, lead-free halide perovskite semiconductors, Chem. Mater. 28 (2016) 1348–1354.
- [45] R.S. Lamba, P. Basera, S. Singh, S. Bhattacharya, S. Sapra, Lead-free alloyed double-perovskite nanocrystals of Cs₂(Na_xAg_{1-x})BiBr₆ with tunable band gap, J. Phys. Chem. C. 125 (2021) 1954–1962.
- [46] Y. Meng, T. Jia, Z. Huang, C. Liu, B. Xie, S. Xia, T. Sakurai, Preparation and photocatalytic properties of multicomponent Nickel-containing organic-inorganic hybrid materials based on ZnCr-LDHs, J. Phys. Chem. Solids 183 (2023) 111644.
- [47] J. Hu, X. Xiong, W. Guan, Y. Chen, H. Long, Design and construction of core-shelled Co₃O₄-CoFe₂O₄ heterojunction for highly sensitive and selective detection of ammonia, Chem. Eng. J. 452 (2023) 139346.
- [48] J. Wang, H. Cheng, D. Wei, Z. Li, Ultrasonic-assisted fabrication of Cs₂AgBiBr₆/ Bi₂WO₆ S-scheme heterojunction for photocatalytic CO₂ reduction under visible light, Chin. J. Catal. 43 (2022) 2606–2614.
- [49] T. Kanata-Kito, M. Matsunage, H. Takakura, Y. Hamakawa, T. Nishino, Photoreflectance characterization of built-in potential in MBE-produced as-grown GaAs surface(100). J. Appl. Phys. 68 (1990) 5309–5313.
- [50] F. Le Formal, K. Sivula, M. Grätzel, The transient photocurrent and photovoltage behavior of a hematite photoanode under working conditions and the influence of surface treatments. J. Phys. Chem. C. 116 (2012) 26707–26720.
- [51] S. Wang, W. Jiang, W. Cui, W. Jiang, M. Zhao, J. Sun, B. Liu, X. Lai, K. Shi, K. Pan, Improved optical properties of lead-free double perovskite Cs₂AgBiBr₆ nanocrystals via Na ions doping, Adv. Opt. Mater. 11 (2023) 2202745.
- [52] N. Ding, L. Shao, T. Xie, G. Pan, D. Zhou, X. Bai, S. Lu, J. Hu, J. Zhou, W. Xu, H. Song, Highly-sensitive, stable, and fast-response lead-free Cs₂AgBiBr₆ double perovskite photodetectors enabled by synergistic engineering of doping Na⁺/Ce³⁺ and integrating ag nanoparticles film, Laser Photonics Rev. 16 (2022) 2200301.
- [53] Q.-M. Sun, J.-J. Xu, F.-F. Tao, W. Ye, C. Zhou, J.-H. He, J.-M. Lu, Boosted inner surface charge transfer in perovskite nanodots@mesoporous titania frameworks for efficient and selective photocatalytic CO₂ reduction to methane, Angew. Chem. Int. Ed. 134 (2022) e202200872.
- [54] P. Liu, Z. Huang, X. Gao, X. Hong, J. Zhu, G. Wang, Y. Wu, J. Zeng, X. Zheng, Synergy between palladium single atoms and nanoparticles via hydrogen spillover for enhancing CO₂ photoreduction to CH₄, Adv. Mater. 34 (2022) 2200057.
- [55] Z.-Z. Wu, X.-L. Zhang, Z.-Z. Niu, F.-Y. Gao, P.-P. Yang, L.-P. Chi, L. Shi, W.-S. Wei, R. Liu, Z. Chen, S. Hu, X. Zheng, M.-R. Gao, Identification of Cu(100)/Cu(111) interfaces as superior active sites for CO dimerization during CO₂ electroreduction, J. Am. Chem. Soc. 144 (2022) 259–269.
- [56] S. Rousseau, O. Marie, P. Bazin, M. Daturi, S. Verdier, V. Harle, Investigation of methanol oxidation over Au/catalysts using operando IR spectroscopy: Determination of the active sites, intermediate/spectator species, and reaction mechanism, J. Am. Chem. Soc. 132 (2010) 10832–10841.
- [57] A.A. Peterson, F. Abild-Pedersen, F. Studt, J. Rossmeisl, J.K. Nørskov, How copper catalyzes the electroreduction of carbon dioxide into hydrocarbon fuels[†], Energy Environ. Sci. 3 (2010) 1311–1315.
- [58] X. Li, Y. Sun, J. Xu, Y. Shao, J. Wu, X. Xu, Y. Pan, H. Ju, J. Zhu, Y. Xie, Selective visible-light-driven photocatalytic CO₂ reduction to CH₄ mediated by atomically thin CuIn₅S₈ layers, Nat. Energy 4 (2019) 690–699.
- [59] D. He, Q. Wang, Y. Rong, Z. Xin, J.-J. Liu, Q. Li, K. Shen, Y. Chen, Sub-nanometer mono-layered metal-organic frameworks nanosheets for simulated flue gas photoreduction, Adv. Mater. 36 (2024) 2403920.
- [60] J. Wang, H. Zhang, Y. Nian, Y. Chen, H. Cheng, C. Yang, Y. Han, X. Tan, J. Ye, T. Yu, Disruption symmetric crystal structure favoring photocatalytic CO₂ reduction: Reduced *COOH formation energy barrier on al doped CuS/TiO₂, Adv. Fun. Mater. 34 (2024) 2406549.
- [61] H. Yuan, A. Krishna, Z. Wei, Y. Su, J. Chen, W. Hua, Z. Zheng, D. Song, Q. Mu, W. Pan, L. Xiao, J. Yan, G. Li, W. Yang, Z. Deng, Y. Peng, Ligand-bound CO₂ as a nonclassical route toward efficient photocatalytic CO₂ reduction with a Ni N-confused porphyrin, J. Am. Chem. Soc. 146 (2024) 10550.